Corrosion Science 80 (2014) 350–358

Contents lists available at ScienceDirect

Corrosion Science

journal homepage: www.elsevier.com/locate/corsci

Stress corrosion cracking under low stress: Continuous or discontinuous cracks?

Longkui K. Zhu [a], Yu Yan [a], Jinxu X. Li [a], Lijie J. Qiao [a,*], Alex A. Volinsky [b,a]

[a] Corrosion and Protection Center, Key Laboratory for Environmental Fracture (MOE), University of Science and Technology Beijing, Beijing 100083, People's Republic of China
[b] Department of Mechanical Engineering, University of South Florida, Tampa, FL 33620, USA

ARTICLE INFO

Article history:
Received 28 June 2013
Accepted 29 November 2013
Available online 5 December 2013

Keywords:
A. Stainless steel
B. SEM
B. Modelling studies
C. Stress corrosion
C. Anodic dissolution

ABSTRACT

Two-dimensional and three-dimensional crack morphologies of stress corrosion cracking (SCC) were studied by serial-sectioning and synchrotron-based X-ray computed tomography. Discontinuous surface cracks were actually continuous inside the specimen, which matched typical river-like fractographs and finite element simulations. A low stress SCC model was created, where a main crack continuously grew along the main propagation direction (MPD) due to anodic dissolution; then, discontinuous secondary microcracks emanated from MPD, angularly extending to the two sides of MPD. Finally, some of the secondary microcracks reached the sample surface, resulting in the formation of discontinuous surface cracks.

1. Introduction

Transgranular stress corrosion cracking (TGSCC) is a typical fracture mode for the SCC system of stainless steels in chloride environments, characterized by river-like fractographs [1–5]. It has been reported that the environmental fracture is discontinuous at the micron scale [4]. Recently, two-dimensional (2-D) detection of TGSCC has indicated that surface cracks in fact nucleate discontinuously and then can connect with each other through breaking of the ligaments between the main crack and the microcracks, especially at the low stress levels [6–8]. In order to elucidate the controlling electrochemical/physical mechanism of the cleavage-like fracture, a corrosion-enhanced plasticity model (CEPM) has been proposed. In CEPM the local stresses increase due to dislocation pile-ups, while the critical stress intensity factor, K_{IC}, decreases due to hydrogen, leading to the microcracks initiation in front of the main crack tips, which finally results in the formation of the river-like fractographs [2–4,9,10]. The 2-D discontinuity of the TGSCC propagation is experimentally and theoretically proven to be reasonable. However, TGSCC is a three-dimensional (3-D) process. To understand the mechanism and more accurately predict the crack growth, it is essential to examine inner geometrical features of discontinuous surface TGSCC cracks.

Inside the specimen, it is a critical issue whether the fracture process is continuous or discontinuous. In theory, apart from the discontinuity, suggested by CEPM, it is also possible for microcracks to initiate continuously when the crack propagation is controlled by anodic dissolution (AD). Numerous experimental results have shown that SCC under low stress should be attributed to an AD mechanism. For example, anodic polarization accelerated SCC [11–13]. The normalized threshold stress intensity factor of SCC, K_I/K_{ISCC}, was much lower than that of hydrogen induced cracking, K_I/K_{IH} [14,15], and most SCC cracks originated from the pits [16–19]. The slip-dissolution model, sometimes called the film-rupture model, has been developed and is referred to as a relatively mature and successful attempt to rationalize the kinetics of SCC [20]. It postulates that either emerging slip planes or simply exposing fresh metal surfaces by rupturing protective films act as anodes. This speeds up metal dissolution prior to re-appearance of the planes, or re-establishment of protective films, while repetition of this sequence makes the cracks longer [20–26]. Hall [25,26] further pointed out that SCC was active path corrosion, assisted by yielding or film rupture. From this perspective, there should be an existing AD path, and TGSCC is continuous inside the samples, which is completely different from the CEPM predictions. Therefore, the inner SCC cracks continuity or discontinuity determines the primary fracture mechanism.

Several researchers have recently addressed 3-D SCC cracks. Marrow et al. [27–29] systematically studied intergranular SCC of a sensitized austenitic stainless steel by means of 2-D fractography and 3-D X-ray computed tomographic images. They found that the discontinuous surface crack was actually continuous within the specimen. However, few experimental efforts have addressed

* Corresponding author. Address: Corrosion and Protection Center, Key Laboratory for Environmental Fracture (MOE), University of Science and Technology Beijing, Beijing 100083, People's Republic of China. Tel.: +86 10 6233 4499; fax: +86 10 6233 2345.
E-mail addresses: lqiao@ustb.edu.cn (L.J. Qiao), volinsky@usf.edu (A.A. Volinsky).

0010-938X/$ - see front matter © 2013 Elsevier Ltd. All rights reserved.
http://dx.doi.org/10.1016/j.corsci.2013.11.057

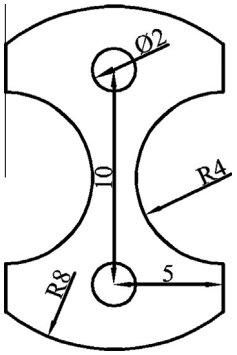

Fig. 1. Schematics of 316L stainless steel single crystal specimens (dimensions in mm).

how the inner TGSCC cracks advance and how the surface discontinuous cracks form. This work aims to detect the continuity or discontinuity of crack propagation paths inside the specimens and attempts to construct a model of TGSCC. In general, approaches to inner crack morphology characterization can be grouped into two categories: destructive serial-sectioning [23,30] and nondestructive X-ray computed tomography [27–29]. The former offers high-resolution slices, while the latter presents the benefits of in situ 3-D visualization of cracks. In this work, both methods have been used to illustrate the TGSCC propagation.

2. Experimental procedure

2.1. SCC test

316L SS single crystals were used in this study with the following chemical composition: C-0.007 wt.%, Cr-17.00 wt.%, Ni-13.49 wt.%, Mo-2.54 wt.%, Mn-0.66 wt.%, Si-0.46 wt.%, P-0.0080 wt.%, S-0.0056 wt.%, Fe-balance. The crystals were produced along [0 0 1] direction and machined into 0.7 mm thick specimens with 2 mm circular holes. Prior to the experiments, the specimens were annealed at 1050 °C for 30 min in argon, water-quenched, followed by grinding to 2000 grit, and were electrochemically thinned to about 0.5 mm in solutions containing H_3PO_4, H_2SO_4, CrO_3 and glycol ($C_2H_6O_2$). Finally, the samples were degreased with acetone in an ultrasonic cleaner and washed with deionized water. The specimen geometry is shown in Fig. 1. After the pretreatment, the samples were placed into a glass container filled with a boiling 45 wt.% $MgCl_2$ solution. A low nominal stress of 20 MPa, calculated according to the narrowest section (2×0.5 mm^2), was applied to the specimen. All experiments were carried out under an open circuit condition, using a weight-type constant load apparatus equipped with a cooling system, two 316L SS single crystal rods and two silica grips. After testing, each specimen was ultrasonically cleaned in deionized water as well as a 5 wt.% HCl + 2 g L^{-1} hexamethylenetetramine mixture, and then TGSCC cracks and fractographs were observed by scanning electron microscopy (SEM) and optical microscopy.

2.2. Approaches to inner crack morphology characterization

Both destructive serial-sectioning and nondestructive X-ray computed tomography were utilized to directly observe the inner discontinuous surface cracks. First, surface layers of the specimens were removed via mechanical polishing and the cracks were observed in SEM. In this way, a series of 2-D cracks at different distance beneath the specimen top surface were obtained and compared to determine whether the cracks were continuous or not. Second, the X-ray computed tomography was used to directly visualize 3-D morphologies of discontinuous surface cracks. To perform tomographic imaging, samples with cracks (about 0.5×0.5 mm^2 cross-sections) were prepared by the following method: wire-electrode cutting; rinsing in acetone; cleaning in deionized water; hot air drying and storing in a desiccated chamber. Subsequently, the computed tomographic experiments were conducted using the BL13W1 beam line at the Shanghai Synchrotron Radiation Facility (SSRF). Almost monochromatic X-ray beam was used with the energy of 42 keV, and a high-speed camera recorded transmitted intensity in an 8 s exposure/projection interval, while the sample was rotated in 0.25° increments. During each 180° rotation, 720 2-D radiographs were recorded and applied to the reconstruction of image slices nearly perpendicular to the crack growth direction. Isotropic voxels with the resolution of 0.7 μm were achieved in the reconstructed slices. Next, image analysis, visualization and 3-D rendering were carried out using a commercial software package (Amira). The whole X-ray computed tomographic process is illustrated in Fig. 2. Additionally, the fractograph was also detected to verify the 3-D crack morphology along with the continuity or the discontinuity of the cracks.

2.3. Finite element analysis

ABAQUS V6.10-1 was used to simulate the stress and strain distribution near the fronts of 3-D crack tips with and without a defect. To simplify the calculation, a 3-D equivalent rectangular specimen was modeled with the dimensions of $2 \times 10 \times 0.5$ mm^3, and a 0.3×0.1 mm^2 semi-elliptic through crack (the half length of the axis in the direction "1" × the half length of the axis in the direction "2") was created at the center of the specimen length in the direction "2", shown in Fig. 3. Due to geometric symmetry, a half of the model was used, shown in Fig. 3(a). Then, an initial defect was cut at the crack front of the pre-cracked specimen. The shape of the initial defect was obtained by rotating a 0.06×0.04 mm^2 semi-ellipse (the half length of the axis in the direction "1" × the half length of the axis in the direction "3" (the thickness direction)) about the crack front, as shown in Fig. 3(c). In this model, the half length of the defect axis in the direction "3" was changed from 0.04 mm to 0.14 mm in order to investigate the effect of the defect size on the stress and strain distribution. For the models with and without the defect, the mesh was created using the 3-D elements C3D20, which are quadratic 20-node elements. The boundary conditions were as follows:

$$\begin{aligned} y = 5, \quad u_y = 0.0005 \\ y = 0, \quad u_y = 0 \end{aligned} \tag{1}$$

The Young modulus of 188 GPa and Poisson's ratio of 0.3 for 316L SS single crystal were the input parameters for the FE model. The normal stress, S_{22}, and the normal strain, LE_{22}, along the tensile direction were used in the analysis to characterize the mechanical behavior of this material.

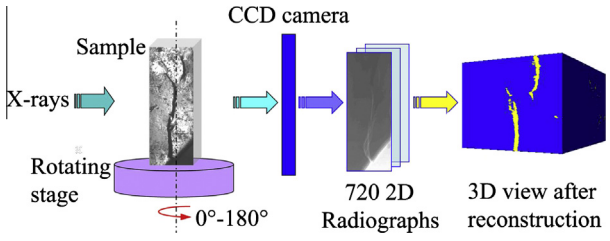

Fig. 2. Schematic diagram of the whole X-ray computed tomographic process.

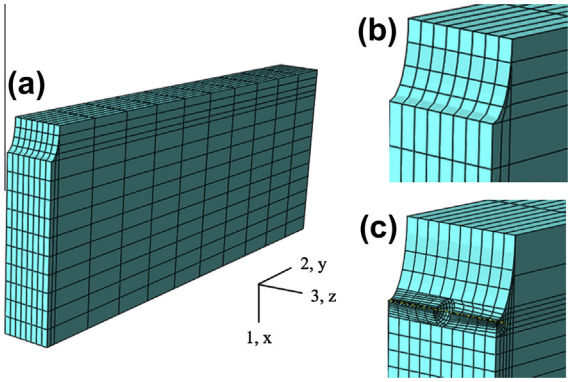

Fig. 3. (a) The half of the equivalent 3-D cracked specimen for the finite element analysis; (b) mesh structure around the crack front without a defect; and (c) mesh structure around the crack front with a defect.

3. Experimental results

3.1. 2-D TGSCC crack morphologies

Many discontinuous surface cracks were observed when the specimens were loaded with 20 MPa stress, as shown in Figs. 4–7(a). Serial-sectioning was carried out to verify whether the cracking was continuous or discontinuous inside the specimens. A set of 2-D TGSCC crack morphologies on side surfaces or cross-sections was obtained. The side surfaces in Figs. 4(a), 5(a), 6(a) and 7(a) were defined as the reference planes of Crack I, II, III and IV, respectively. Fig. 4 shows the morphologies of Crack I on the side surface and the cross-sections at different distance away from the reference plane. Six discontinuous microcracks connected with the ligaments were observed at the middle part of Crack I in Fig. 4(a). When a 6 μm thick surface layer was removed, the ligaments in Fig. 4(b) became narrower. Almost all the ligaments disappeared and Crack I became continuous when the specimen was polished further, 28 μm deeper than the reference plane, as shown in Fig. 4(c). Another specimen was examined in the same way, as shown in Fig. 5. Discontinuous microcracks "1" to "14" on the side surface are seen in Fig. 5(a). The microcracks "1" to "10" connected with each other on the cross-section 200 μm deeper than the reference plane, as seen in Fig. 5(b). Four ligaments between adjacent microcracks "10" to "14" in Fig. 5(a) coalesced into one ligament in Fig. 5(b) and then completely disappeared when the specimen was polished 342 μm deeper than the reference plane, as seen in Fig. 5(c). That is, the discontinuous middle part of Crack II on the side surface was partially continuous close to the mid-thickness of the specimen and was fully continuous on the cross-section 342 μm deeper than the reference plane.

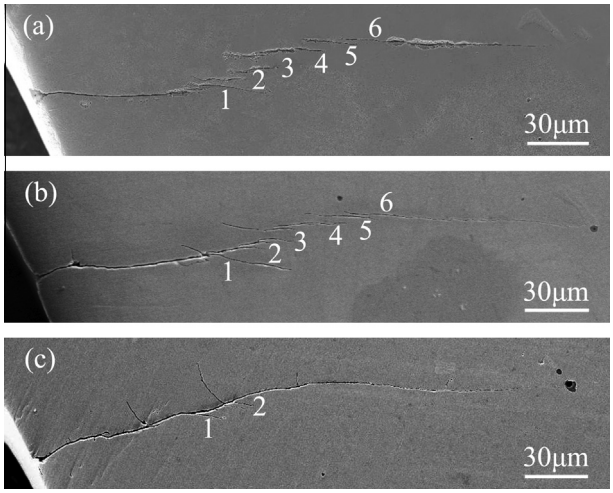

Fig. 4. SEM morphologies of Crack I on a side surface and cross-sections: (a) 0 μm; (b) 6 μm and (c) 28 μm deeper than the reference surface in (a).

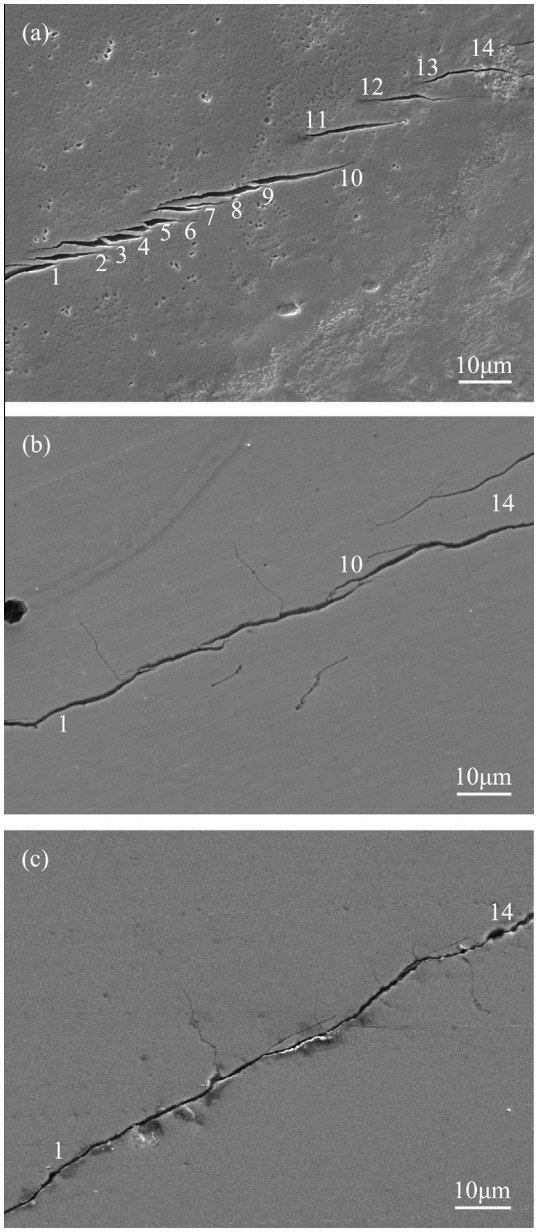

Fig. 5. Partial SEM morphologies of Crack II on a side surface and cross-sections: (a) 0 μm; (b) 200 μm and (c) 342 μm deeper than the reference surface in (a).

Fig. 6(a) exhibits the magnified morphologies of the tip of Crack III on the side surface. The ligaments far away back from the crack tip were broken and the microcracks close to the crack tip were still discrete. However, after only 6 μm thick surface layer has been removed, Crack III appeared continuous on the new cross-section in Fig. 6(b). To verify the inner continuity, another specimen with discontinuous microcracks was examined by SEM. The whole 2-D morphology of the tip of Crack III from the outside to the inside of the specimen is shown in Fig. 7. The microcracks in Fig. 7(a–e) were disconnected from the surface to the depth of 231 μm, and the width of the ligament in Fig. 7(b) was greater than that on the other cross-sections. This indicates that a change from discontinuity to continuity possibly occurred within 53 μm away from

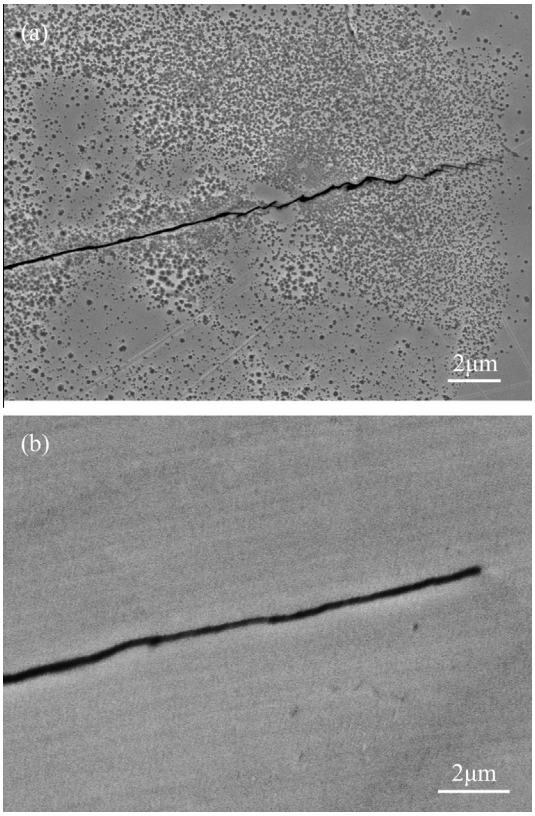

Fig. 6. SEM morphologies of the tip of Crack III on a side surface and a cross-section: (a) 0 μm and (b) 6 μm deeper than the reference surface in (a).

the reference plane. Then, the width of the ligaments decreased from Fig. 7(c–e). Finally, it was obviously continuous on the cross-sections in Fig. 7(f and g) and the other side surface in Fig. 7(h), which was analogous to the tip of Crack III in Fig. 6(b).

As a result, 2-D crack morphologies via serial-sectioning demonstrate that the discontinuous TGSCC cracks on the surfaces were actually continuous inside the specimens.

3.2. 3-D TGSCC crack morphologies

In order to obtain the 3-D crack morphology, a specimen was tested in the boiling 45% $MgCl_2$ solution at the same 20 MPa stress. The test was stopped when a small crack could be observed. This crack is denoted as the Crack V. The surface morphology and the fractograph of the Crack V were characterized by SEM, as shown in Fig. 8. The 3-D morphology of the Crack V between the dotted lines "1" and "2" and the region between the dotted lines "2" and "3" in Fig. 8 were obtained by means of synchrotron-based X-ray computed tomography, as shown in Fig. 9(a and b), respectively. It has been found that a small ligament "L1" was located on the side surface between the dotted lines "1" and "2" in Fig. 8(a). However in Fig. 9(a), two parts of the crack, separated by the ligament, gradually approached from the outside to the inside and finally connected with each other inside the specimen, meaning that the ligament became gradually smaller. Then, the specimen was torn along the crack. Although the ligament was dropped out from the fractograph in Fig. 8(c), a tiny topography fluctuation was examined at the right edge of the fractograph. It originated from an inner site and propagated to the right edge, which matched well with the 3-D morphology of the middle part of the Crack V in Fig. 9(a). Next, the 3-D feature of the tip of the Crack V was characterized, as shown in Figs. 8 and 9(b). Two discrete crack sections split by the ligament "L2" on the side surface between the dotted lines "2" and "3" in Fig. 8(a) linked with one another inside the specimen in Fig. 9(b). Likewise, this kind of external discontinuity and internal continuity phenomenon was explicitly reflected in the fractograph in Fig. 8(c). A protrusion at the right edge was just the ligament "L2". It initiated at an inner point and gradually propagated to the right edge. This directly results in the formation of the discontinuous tip of the Crack V on the surface. In conclusion, the 3-D crack morphology and the 2-D fractograph of the different parts of the Crack V indicate that the discontinuous TGSCC crack continuously propagated inside the specimen, and the surface microcracks were separated by the ligaments, which were responsible for the surface discontinuity of the Crack V.

3.3. TGSCC fractographs

Fig. 10 shows a typical river-like TGSCC fractograph and the discontinuous surface microcracks of the austenitic stainless steel in the boiling $MgCl_2$ solution. It has been found that the area marked by dotted lines was smooth and continuous, approximately from several to more than ten microns in width, defined as a macroscopic propagation direction (MPD). A number of secondary cracks and steps, marked by arrows, emanated from MPD and were extended to the two sides of MPD at an angle. Obviously, some of them reached the edge of the fractograph, leading to the formation of the surface discrete microcracks "1" to "7", as shown in Fig. 10(a). The same cracking phenomenon is also seen in Fig. 8(c). Inconspicuous MPD close to the mid-width of the Crack V fractograph acted as the nucleation site of numerous secondary cracks and steps. Then, the angled extension of a few secondary cracks and steps resulted in the formation of the discontinuous surface Crack V in Fig. 8(a). As a consequence, continuous MPDs directly caused the inner TGSCC continuity at the micron scale, while the microscopic surface TGSCC discontinuity was immediately induced by the secondary cracks and steps emanating from MPDs. In addition, it has also been found that the front of the Crack V was not a straight line, and two similar pitting defects, marked by arrows, were distributed at the front of MPD in Fig. 8(c).

3.4. Stress and strain distribution

The main cracks propagated along MPDs inside the specimens, and then the secondary cracks originated from MPDs, forming the fishbone-shaped SCC crack morphologies and the discontinuous surface microcracks. In order to explain the phenomenon, FE method was used to calculate the normal stress, S_{22}, and the normal strain, LE_{22}, distributed near the fronts of 3-D equivalent cracks. As seen in Fig. 11(a and b), the peak values of S_{22} and LE_{22} emerged near the mid-thickness of the crack front. Numerically, S_{22} and LE_{22} near the mid-thickness were 91.8 MPa and 0.042%, respectively, while the corresponding values on the edge were 72 MPa and 0.035%, as shown in Fig. 11(c). This means that the main crack would propagate preferentially near the mid-thickness and a microcrack similar to a defect could be formed. Then, a defect was embedded into the mid-thickness of the crack front to simulate the stress and strain distribution for the preferential propagation. Both S_{22} and LE_{22} concentration points simultaneously moved to two shoulders of the defect and their minima along the crack front appeared at the defect bottom, as seen in Fig. 12(a and b). The quantitative results in Fig. 12(c) illustrate that S_{22} and LE_{22} at the defect shoulders were 211.6 MPa and 0.111%, respectively, and correspondingly, the values at the defect bottom were 70.7 MPa and 0.036%. When the applied elastic strain and the length of the defect axis in the direction "1" were kept constant, it was found that S_{22} and LE_{22} at the defect shoulders gradually

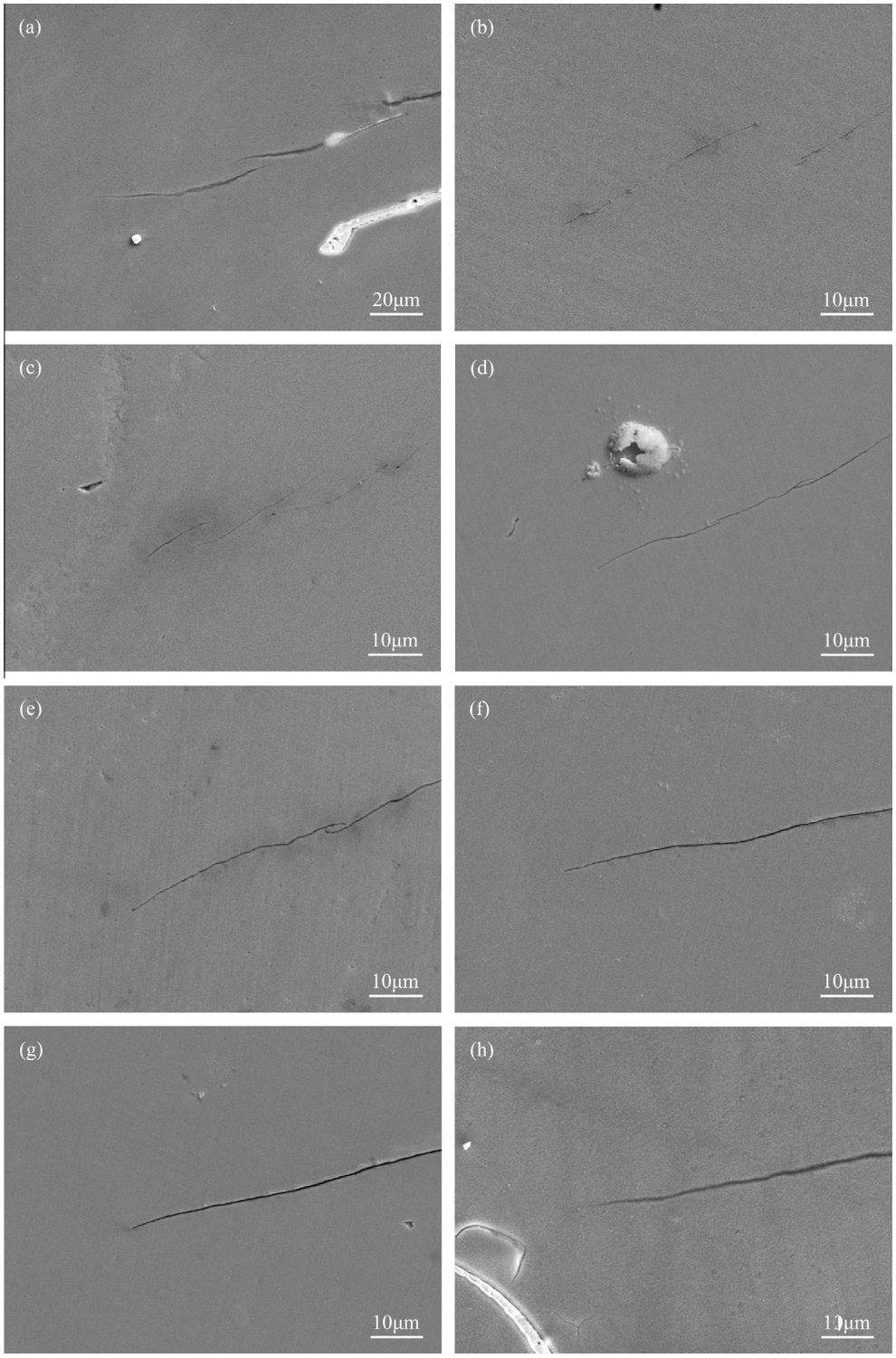

Fig. 7. SEM morphologies of the tip of Crack IV on side surfaces and cross-sections: (a) 0 μm; (b) 53 μm; (c) 109 μm; (d) 159 μm; (e) 231 μm; (f) 291 μm; (g) 335 μm and (h) 470 μm deeper than the reference surface in (a).

increased with the defect growing along direction "3", as shown in Fig. 13. Quantitatively, S_{22} increased from 211.6 MPa to 297.8 MPa and LE_{22} increased from 0.111% to 0.156% when the defect axis length in the direction "3" changed from 0.04 mm to 0.14 mm. The new stress and strain distribution will result in the secondary crack initiation at the defect shoulders and the propagation to both sides of MPD.

4. Modeling of TGSCC

4.1. The formation of MPD

TGSCC microscopic process is synergistically controlled by AD, hydrogen and local stresses, when specimens are subjected to low stresses in corrosive environments [4,5,11,12]. One of the most

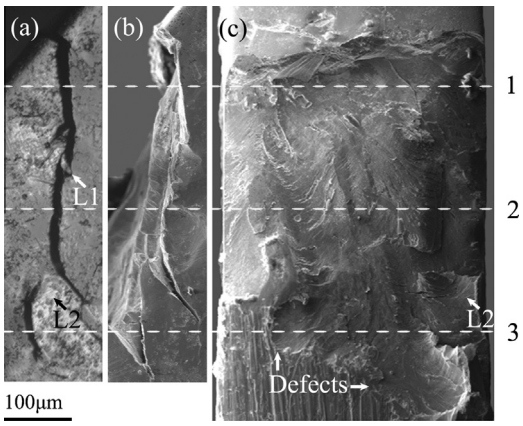

Fig. 8. (a) Optical micrograph of the Crack V on the side surface of the specimen by wire-electrode cutting; (b) partial SEM morphology of the crack after the specimen was pulled apart along the crack; (c) SEM fractograph of the Crack V.

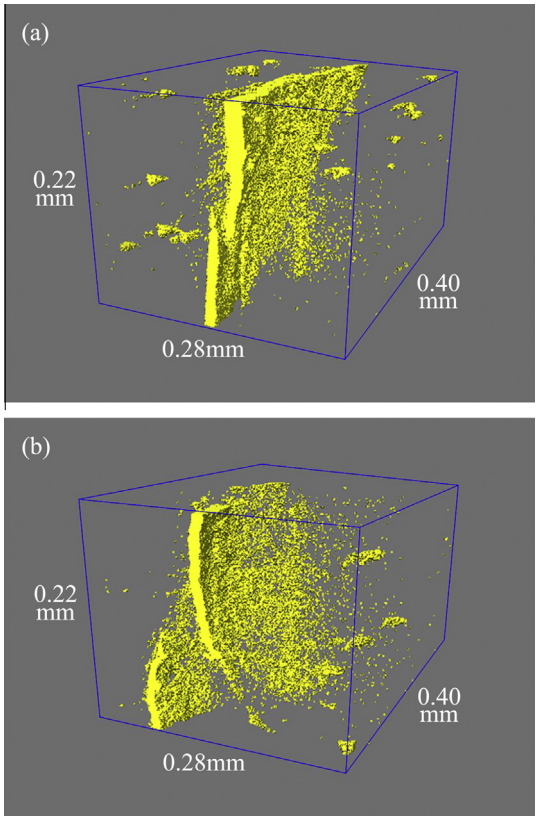

Fig. 9. 3-D rendering of the Crack V: (a) between the dotted lines "1" and "2"; (b) between the dotted lines "2" and "3" in Fig. 8, where the crack is indicated in yellow. (For interpretation of the references to colour in this figure legend, the reader is referred to the web version of this article.)

representative phenomena, shown in Fig. 14(a), is MPD present on almost all river-like fractured surfaces of the austenitic stainless steel in boiling $MgCl_2$ solutions. Our experimental results indicate that the discontinuous surface TGSCC cracks were continuous and originated from MPDs within the specimens. It is considered that MPD results from an AD mechanism. However, Magnin et al. [4] suggested that MPD was possibly induced by the linear combination of two slip systems. It may be a reasonable mechanism if the shear stress, τ, along the slip direction exceeds the critical resolved shear stress, τ_C, making a slip system start. The shear stress, τ, is given by

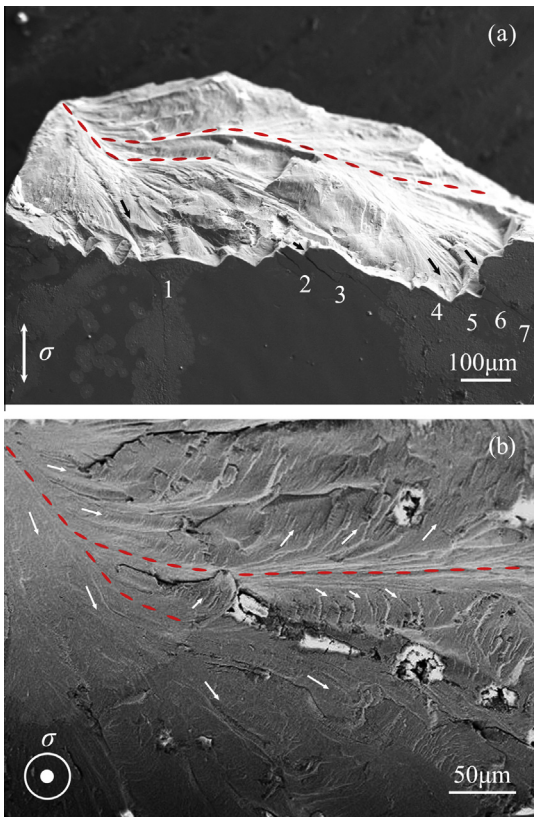

Fig. 10. (a) Microcracks "1" to "7" on a side surface of 316L stainless steel single crystal and (b) typical river-like fractograph of the same area in (a), where the area marked by dotted lines is defined as MPD and a number of discontinuous secondary cracks and steps marked by arrows emanated from MPD and angularly extended to both sides of MPD, leading to the formation of the discontinuous surface microcrack.

$$\tau = \sigma \cos\phi \cos\lambda \tag{2}$$

where σ is the applied stress; ϕ is the angle between the applied stress and the normal line of the {1 1 1} slip plane; λ is the angle between the applied stress and the ⟨1 1 0⟩ slip direction; and $\cos\phi \cos\lambda$ is the Schmidt factor with the maximum of 0.5. In view of the local stress concentration, substituting the maximum stress, σ_{max} = 42.8 MPa [31], and the maximum Schmidt factor, $(\cos\phi \cos\lambda)_{max}$ = 0.5, yields the maximum shear stress, τ_{max} = 21.4 MPa. For 316L austenitic stainless steel, τ_C is approximately 3.2×10^{-4} of the shear modulus, $G = E/2(1+\nu) = 188/2(1+0.3)$ GPa = 72 GPa [32], about 23 MPa and slightly greater than τ_{max}. Thus, the slip system is difficult to start along the ⟨1 1 0⟩ slip direction on the {1 1 1} slip plane in this kind of loading configuration. Then, with the crack growth, the slip system possibly starts because the local stress gradually increases at the crack tip under constant load. That is, MPD is probably formed by the linear combination of the two slip systems. In this way, tear ridges at intersections should be examined along the MPD. Nevertheless, MPDs obtained in Figs. 8(c) and 10 were smooth and continuous. Consequently, MPD could not be induced by these two {1 1 1}⟨1 1 0⟩ slip systems in the process of TGSCC propagation.

In essence, TGSCC is an electrochemical process, in which fresh surfaces, assisted by yielding or film rupture, act as anodes and dissolve at a 3-D crack tip [20–26]. Since the stress gradient exits along the crack front and the maximum value appears near the mid-thickness, yielding or film rupture assisted corrosion tends to take place inside the specimen rather than on the side surfaces. On the other hand, based on the autocatalysis theory in the

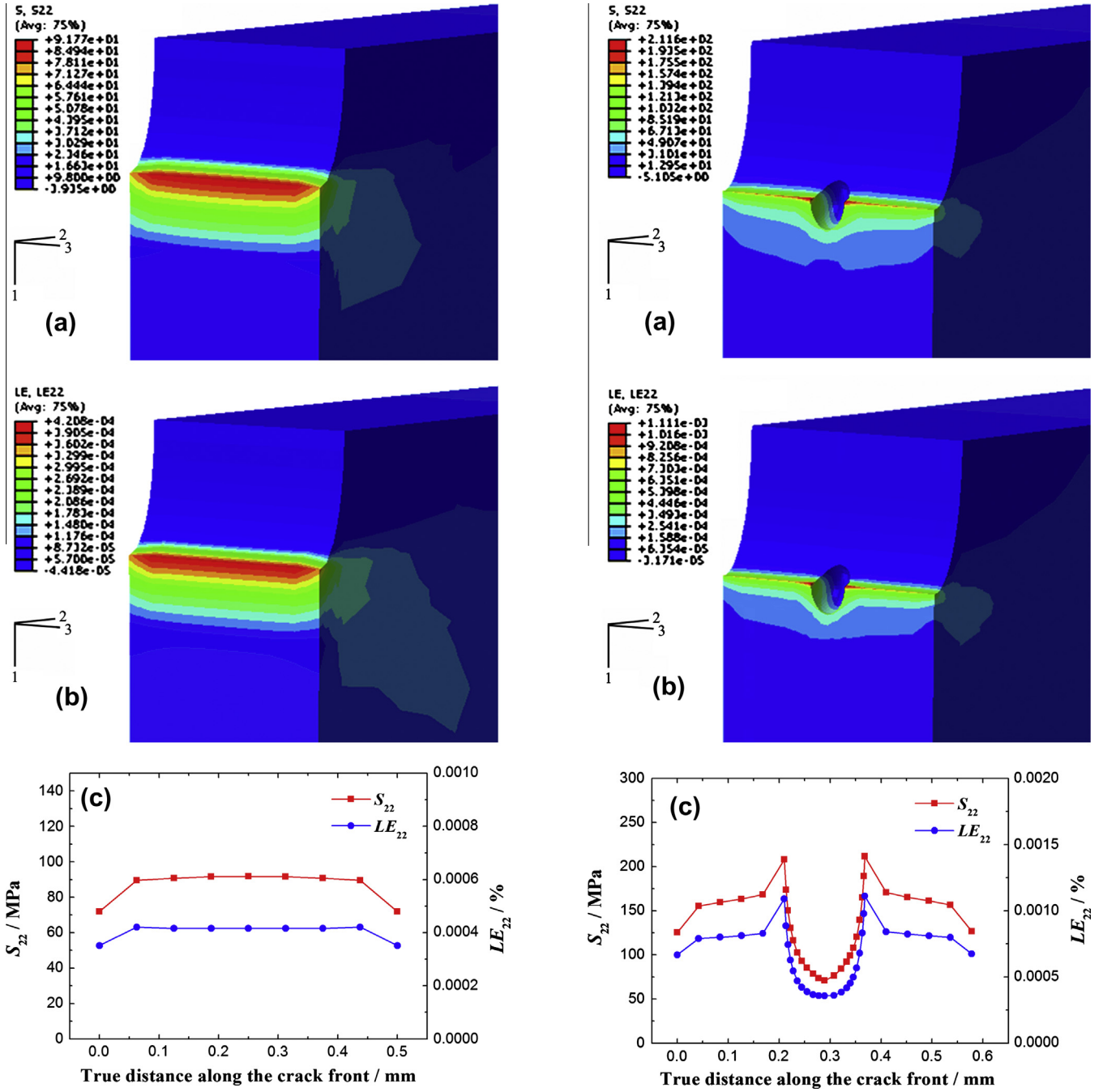

Fig. 11. Distribution of (a) the normal stress, S_{22}, and (b) the normal strain, LE_{22}, around the 3-D crack front without a defect; (c) S_{22} and LE_{22} along the crack front.

Fig. 12. Distribution of (a) the normal stress, S_{22} and (b) the normal strain, LE_{22}, around the 3-D crack front with a defect; (c) S_{22} and LE_{22} along the crack front.

occluded cell, the pH value decreases inside the crack tip, owing to the hydrolysis of metal ions, which facilitates the electrochemical process within the specimen. Thus, MPD induced by the AD mechanism is often inside the specimen. Based on the Faraday's law, the instantaneous crack growth rate, $\dot{a}$, in MPD can be expressed as a function of the instantaneous anodic current density, i_a,

$$\dot{a} = \frac{M}{z\rho F} i_a \tag{3}$$

where M is the molecular weight; z is the charge of the metal cation; ρ is metal density; F is the Faraday's constant. The instantaneous anodic current density, i_a, is related to a partially activated surface, and can be expressed as a product of the current density of the activated surface, i_a^*, and the activated area fraction, A, [26]

$$i_a = i_a^* A \tag{4}$$

In order to simplify calculations, A is given by

$$A = \frac{B_{MPD}}{B_0} \tag{5}$$

where B_{MPD} is the instantaneous width of MPD in the river-like fractograph; B_0 is the specimen thickness. Combining Eqs. (3)–(5), the instantaneous crack growth rate can be written as a function of B_{MPD}

$$\dot{a} = \frac{M i_a^*}{z\rho F B_0} B_{MPD} \tag{6}$$

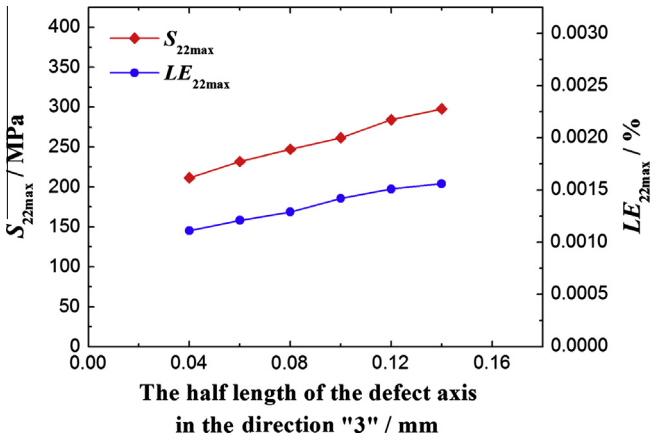

Fig. 13. Variation of the maximum normal stress, S_{22max}, and the maximum normal strain, LE_{22max}, at the defect shoulders vs. the half length of the defect axis in the direction "3".

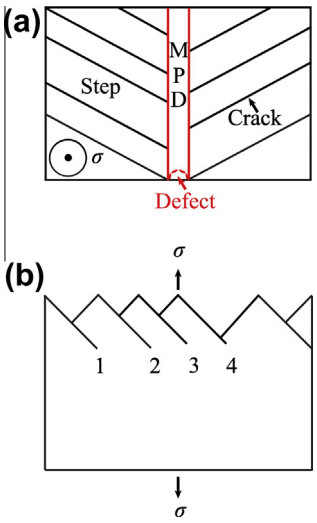

Fig. 14. Model of the TGSCC process: (a) the main crack continuously grows along MPD, then discontinuous secondary microcracks and microsteps emanate from MPD, and instantaneously, secondary microcracks nucleate at or near the two shoulders of a defect; and (b) some of the secondary microcracks and microsteps reach the side surface, resulting in the formation of discontinuous surface cracks and ligaments, such as Crack "1" to "4" and the ligaments between the cracks.

Consequently, the TGSCC crack growth rate in MPD depends on B_{MPD} when temperature and electrochemical environment are kept constant inside the crack tip. For 316L specimens, $M = 56.46\ g\ mol^{-1}$, $z = 2.76$, $\rho = 7.9 \times 10^{-3}\ g\ cm^{-3}$, $B_0 = 0.5$ mm, $B_{MPD} = 10\ \mu m$ and $i_a^* \approx 10 - 100\ mA\ cm^{-2}$ [12,26]. Substituting M, z, ρ, B_0, B_{MPD}, i_a^* and $F = 96{,}500\ C\ mol^{-1}$ into Eq. (6) yields the TGSCC crack growth rate $\dot{a} \approx 5.4 \times 10^{-4} - 5.4 \times 10^{-3}\ m\ s^{-1}$.

4.2. Discontinuous surface cracks and steps

Typically, river-like fractograph on TGSCC is composed of MPDs and discontinuous steps. The experiments show that these steps angularly emanated from MPDs. As seen in Fig. 14(a), it is considered that a main crack extended along MPD and an instantaneous pitting defect, i.e. a microcrack was formed at the crack front. Because the maximum normal stress and strain simultaneously appeared at the two shoulders of the defect, one or a few secondary microcracks can nucleate at or near the two stress and strain concentrated sites. Then, the main crack continues to propagate, producing another defect at the front of MPD and other secondary microcracks around two new shoulders. In this way, discontinuous microsteps between the neighboring but unconnected secondary microcracks are formed at the two sides of MPD. In addition, these microsteps and secondary microcracks initiate at a certain angle, possibly affected by the maximum normal stress and strain direction at two MPD's sides.

Afterwards, the microsteps and the secondary microcracks propagated to side specimen surfaces. The process may be controlled by AD, hydrogen and local stresses. With the AD proceeding at crack tips, hydrogen evolution could occur at cathodes owing to acidic environment inside the crack tips [33]. The reaction is represented by

$$H^+ + e \rightarrow H \tag{7}$$

Generally, hydrogen atoms are larger than interstitial sites: $r_H = 0.53$ Å, compared with $r_i = 0.19$ Å for octahedral sites in the austenitic stainless steel [10]. Thereby, an introduction of hydrogen into lattices led to a distortion of the host lattices and created the hydrogen induced strain, ε_H. Combining ε_H with the strain, ε_{appl}, caused by the applied stress, the total strain, ε, is

$$\varepsilon = \varepsilon_H + \varepsilon_{appl} \tag{8}$$

With the secondary microcracks extending, ε near the crack tips increased under constant load. When the strain-induced shear stresses along $\langle 1\,1\,0 \rangle$ slip directions were greater or equal to τ_C, dislocations emitted on the $\{1\,1\,1\}$ slip planes. After the dislocation emission fully developed, the microcracks initiated and propagated at the front of the crack tips [7]. On the other hand, hydrogen and the local stresses were capable of synergistically promoting AD rates [32], so an AD mechanism could also cause initiation and propagation of microcracks. In any case, it is certain that some of the discontinuous secondary microcracks and microsteps emanating from MPD extend to specimen side surfaces, finally resulting in the formation of discontinuous surface cracks and ligaments in Fig. 14(b).

4.3. The continuity and the discontinuity of TGSCC

It is important but controversial whether the TGSCC process is continuous or discontinuous. CEPM suggests that the synergistic effect of dislocations and hydrogen could cause SCC microcracks to initiate discontinuously ahead of the main crack tips [2–4,9,10], while the slip dissolution model proposes that the process was continuous due to the dissolution of emergent slip planes, or simply exposing fresh metal surfaces [20–26]. The numerous observations in the study show that the discontinuous surface cracks were continuous inside the specimens under low stress, distinguishing the complete continuity proposed by the slip dissolution model as well as the absolute discontinuity suggested by CEPM. It is considered that the inner continuity was induced by the main crack growth along MPD in terms of an AD process at low stress levels. Discontinuous secondary microcracks and microsteps originated from MPD and angularly propagated to side specimen surfaces, which led to the surface discontinuity at the micron scale. This is referred to as a TGSCC model at low stress levels. From the perspective of the whole 3-D samples, it is possible that two or more MPDs appeared simultaneously, and one of them possibly distributed near surfaces, not necessarily at the mid-thickness, owing to a small stress difference at the crack fronts. Namely, transition from discontinuity to continuity could occur inside specimens more than once, for instance the tip of Crack IV in Fig. 7. Thereby, to be exact, the whole TGSCC process consists of local continuity in MPDs and local discontinuity among the secondary microcracks and microsteps.

5. Conclusions

2-D and 3-D crack morphologies of the middle parts and the crack tips using serial-sectioning along with synchrotron-based X-ray computed tomography indicate that the discontinuous surface TGSCC cracks were continuous inside the specimens, which coincided with MPDs and the discrete steps in the typically river-like fractographs. This TGSCC phenomenon is different from that suggested by the slip dissolution model and CEPM. To obtain the TGSCC mechanism, FE method was used to simulate the stress and strain distribution of the 3-D crack fronts with and without a defect. It has been found that the normal stress and strain concentrated near the mid-thickness of the crack front without the defect, but their maximum values were transferred to the shoulders rather than the bottom of the defect on the crack front. When the applied elastic strain was kept constant, the peak values increased with the growing defect. The SCC model under low stress was proposed. The main crack continuously grew along MPD due to an AD mechanism; then, discontinuous secondary microcracks and microsteps emanated from MPD, angularly extending to both sides of MPD. Finally, some of the secondary microcracks and microsteps reached the specimen side surfaces, leading to the formation of discontinuous surface cracks and ligaments. This model is suitable for the internally continuous and externally discontinuous cracks obtained in the experiments. Moreover, the whole 3-D TGSCC process is actually composed of local continuity in MPDs and local discontinuity among the secondary cracks and steps, known from complete continuity or absolute discontinuity. The low stress SCC model mentioned above also applies to this type of fracture.

Acknowledgements

The authors wish to thank You He, Yanan Fu and Honglan Xie at the Shanghai Synchrotron Radiation Facility for their experimental help. The authors also want to acknowledge the funding provided by the National Nature Science Foundation of China under Grants Nos. 50731003 and 51171024. AV would like to acknowledge support from the National Science Foundation.

References

[1] L.J. Qiao, X. Mao, J.L. Luo, Micromechanics of stress corrosion cracking of single-crystal austenitic type 321 stainless steel under mode II loading, Corrosion 52 (1996) 927–933.
[2] T. Magnin, R. Chieragatti, R. Oltra, Mechanism of brittle fracture in a ductile 316 alloy during stress corrosion, Acta Metall. Mater. 38 (1990) 1313–1319.
[3] T. Magnin, A. Chambreuil, B. Bayle, The corrosion-enhanced plasticity model for stress corrosion cracking in ductile fcc alloys, Acta Mater. 44 (1996) 1457–1470.
[4] J.P. Chateau, D. Delafosse, T. Magnin, Numerical simulations of hydrogen-dislocation interactions in fcc stainless steels.: Part II: hydrogen effects on crack tip plasticity at a stress corrosion crack, Acta Mater. 50 (2002) 1523–1538.
[5] O.M. Alyousif, R. Nishimura, Stress corrosion cracking and hydrogen embrittlement of sensitized austenitic stainless steels in boiling saturated magnesium chloride solutions, Corros. Sci. 50 (2008) 2353–2359.
[6] L.J. Qiao, K.W. Gao, A.A. Volinsky, X.Y. Li, Discontinuous surface cracks during stress corrosion cracking of stainless steel single crystal, Corros. Sci. 53 (2011) 3509–3514.
[7] J.X. Li, W.Y. Chu, Y.B. Wang, L.J. Qiao, In situ TEM study of stress corrosion cracking of austenitic stainless steel, Corros. Sci. 45 (2003) 1355–1365.
[8] H. Masuda, SKFM observation of SCC on SUS304 stainless steel, Corros. Sci. 49 (2007) 120–129.
[9] W.F. Flanagan, P. Bastias, B.D. Lichter, A theory of transgranular stress-corrosion cracking, Acta Metall. Mater. 39 (1991) 695–705.
[10] J.P. Chateau, D. Delafosse, T. Magnin, Numerical simulations of hydrogen-dislocation interactions in fcc stainless steels.: Part I: hydrogen-dislocation interactions in bulk crystals, Acta Mater. 50 (2002) 1507–1522.
[11] B.E. Wilde, C.D. Kim, The role of hydrogen in the mechanisms of stress corrosion cracking of austenitic stainless steels in hot chloride media, Corrosion 28 (1972) 350–356.
[12] L.J. Qiao, X. Mao, W.Y. Chu, The role of hydrogen in stress corrosion cracking of hot $MgCl_2$ solution, Metall. Mater. Trans. 26A (1995) 1777–1784.
[13] W.W. Wang, Y.J. Su, Y. Yan, J.X. Li, L.J. Qiao, W.Y. Chu, X.K. Wang, Y. Xing, The role of hydrogen in stress corrosion cracking of 310 austenitic stainless steel in a boiling $MgCl_2$ solution, Corros. Sci. 60 (2012) 275–279.
[14] L.J. Qiao, W.Y. Chu, C.M. Hsiao, Delayed fracture of austenitic stainless steel under mode III loading, Scr. Metall. 21 (1987) 7–11.
[15] L.J. Qiao, W.Y. Chu, C.M. Hsiao, J.D. Lu, Stress corrosion cracking and hydrogen-induced cracking in austenitic stainless steel under mode II loading, Corrosion 44 (1988) 50–54.
[16] A. Turnbull, S. Zhou, Pit to crack transition in stress corrosion cracking of a steam turbine disc steel, Corros. Sci. 46 (2004) 1239–1264.
[17] B.J. Connolly, D.A. Horner, S.J. Fox, A.J. Davenport, C. Padovani, S. Zhou, A. Turnbull, et al., X-ray microtomography studies of localized corrosion and transitions to stress corrosion cracking, Mater. Sci. Technol. 22 (2006) 1076–1085.
[18] A. Turnbull, L. Wright, L. Crocker, New insight into the pit-to-crack transition from finite element analysis of the stress and strain distribution around a corrosion pit, Corros. Sci. 52 (2010) 1492–1498.
[19] D.A. Horner, B.J. Connolly, S. Zhou, L. Crocker, A. Turnbull, Novel images of the evolution of stress corrosion cracks from corrosion pits, Corros. Sci. 53 (2011) 3466–3485.
[20] R.C. Newman, C. Healey, Stability, validity and sensitivity to input parameters of the slip-dissolution model for stress-corrosion cracking, Corros. Sci. 49 (2007) 4040–4050.
[21] H.L. Logan, Film-rupture mechanism of stress corrosion, J. Res. Natl. Bur. Stand. 48 (1952) 99–105.
[22] D.A. Vermilyea, A theory for the propagation of stress corrosion cracks in metals, J. Electrochem. Soc. 119 (1972) 405–407.
[23] D.G. Kolman, J.R. Scully, Continuum mechanics characterization of plastic deformation-induced oxide film rupture, Philos. Mag. A 79 (1999) 2313–2338.
[24] E.M. Gutman, An inconsistency in "film rupture model" of stress corrosion cracking, Corros. Sci. 49 (2007) 2289–2302.
[25] M.M. Hall Jr., Critique of the Ford–Andresen film rupture model for aqueous stress corrosion cracking, Corros. Sci. 51 (2009) 1103–1106.
[26] M.M. Hall Jr., Flim rupture model of aqueous stress corrosion cracking under constant and variable stress intensity factor, Corros. Sci. 51 (2009) 225–233.
[27] T.J. Marrow, L. Babout, A.P. Jivkov, P. Wood, D. Engelberg, N. Stevens, P.J. Withers, R.C. Newman, Three dimensional observations and modeling of intergranular stress corrosion cracking in austenitic stainless steel, J. Nucl. Mater. 352 (2006) 62–74.
[28] S.A. Shipilov, R.H. Jones, J.-M. Olive, R.B. Rebak, Environment-Induced Cracking of Materials, Elsevier Science Ltd., Alberta, 2007.
[29] A. King, G. Johnson, D. Engelberg, W. Ludwig, J. Marrow, Observations of intergranular stress corrosion cracking in a grain-mapped polycrystal, Science 321 (2008) 382–385.
[30] S. Lozano-Perez, P. Rodrigo, L.C. Gontard, Three-dimensional characterization of stress corrosion cracking, J. Nucl. Mater. 408 (2011) 289–295.
[31] L.K. Zhu, Y. Yan, L.J. Qiao, A.A. Volinsky, Stainless steel pitting and early-stage stress corrosion cracking under ultra-low elastic load, Corros. Sci. (2013) 360–368, http://dx.doi.org/10.1016/j.corsci.
[32] X.H. Cheng, Q.X. Dai, A.D. Wang, Stacking-fault energy and ε-martensite transformation of austenitic steels, J. Iron Steel Res. 15 (2003) 55–58.
[33] L. Qiao, X. Mao, Thermodynamic analysis on the role of hydrogen in anodic stress corrosion cracking, Acta Metall. Mater. 43 (1995) 4001–4006.